Monthly Notices of the ROYAL ASTRONOMICAL SOCIETY

MNRAS **501,** 1–13 (2021) doi:10.1093/mnras/staa3593
Advance Access publication 2020 November 21

Interpreting LOFAR 21-cm signal upper limits at $z \approx 9.1$ in the context of high-z galaxy and reionization observations

Bradley Greig [1,2★] Andrei Mesinger [3] Léon V. E. Koopmans,[4] Benedetta Ciardi,[5] Garrelt Mellema [6] Saleem Zaroubi,[4,7,8] Sambit K. Giri [9] Raghunath Ghara [7,8] Abhik Ghosh [10] Ilian T. Iliev [11] Florent G. Mertens [4,12] Rajesh Mondal [6,11] André R. Offringa [4,13] and Vishambhar N. Pandey[4,13]

[1]*ARC Centre of Excellence for All-Sky Astrophysics in 3 Dimensions (ASTRO 3D), University of Melbourne, VIC 3010, Australia*
[2]*School of Physics, University of Melbourne, Parkville, VIC 3010, Australia*
[3]*Scuola Normale Superiore, Piazza dei Cavalieri 7, I-56126 Pisa, Italy*
[4]*Kapteyn Astronomical Institute, University of Groningen, PO Box 800, NL-9700 AV Groningen, the Netherlands*
[5]*Max-Planck Institute for Astrophysics, Karl-Schwarzschild-Straße 1, D-85748 Garching, Germany*
[6]*The Oskar Klein Centre, Department of Astronomy, Stockholm University, AlbaNova, SE-10691 Stockholm, Sweden*
[7]*Department of Natural Sciences, The Open University of Israel, 1 University Road, PO Box 808, Ra'anana 4353701, Israel*
[8]*Department of Physics, Technion, Haifa 32000, Israel*
[9]*Institute for Computational Science, University of Zurich, Winterthurerstrasse 190, CH-8057 Zurich, Switzerland*
[10]*Department of Physics, Banwarilal Bhalotia College, GT Rd, Ushagram, Asansol, West Bengal 713303, India*
[11]*Astronomy Centre, Department of Physics and Astronomy, University of Sussex, Pevensey II Building, Brighton BN1 9QH, UK*
[12]*LERMA, Observatoire de Paris, PSL Research University, CNRS, Sorbonne Universite, F-75014 Paris, France*
[13]*ASTRON – the Netherlands Institute for Radio Astronomy, Oude Hoogeveensedijk 4, NL-7991 PD Dwingeloo, the Netherlands*

Accepted 2020 November 11. Received 2020 November 2; in original form 2020 June 4

ABSTRACT

Using the latest upper limits on the 21-cm power spectrum at $z \approx 9.1$ from the Low Frequency Array (LOFAR), we explore the regions of parameter space which are inconsistent with the data. We use 21CMMC, a Monte Carlo Markov chain sampler of 21CMFAST which directly forward models the three dimensional (3D) cosmic 21-cm signal in a fully Bayesian framework. We use the astrophysical parametrization from 21CMFAST, which includes mass-dependent star formation rates and ionizing escape fractions as well as soft-band X-ray luminosities to place limits on the properties of the high-z galaxies. Further, we connect the disfavoured regions of parameter space with existing observational constraints on the Epoch of Reionization such as ultra-violet (UV) luminosity functions, background UV photoionization rate, intergalactic medium (IGM) neutral fraction, and the electron scattering optical depth. We find that all models exceeding the 21-cm signal limits set by LOFAR at $z \approx 9.1$ are excluded at $\gtrsim 2\sigma$ by other probes. Finally, we place limits on the IGM spin temperature from LOFAR, disfavouring at 95 per cent confidence spin temperatures below $\sim$2.6 K across an IGM neutral fraction range of $0.15 \lesssim \bar{x}_{\rm H\,I} \lesssim 0.6$. Note, these limits are only obtained from 141 h of data in a single redshift bin. With tighter upper limits, across multiple redshift bins expected in the near future from LOFAR, more viable models will be ruled out. Our approach demonstrates the potential of forward modelling tools such as 21CMMC in combining 21-cm observations with other high-z probes to constrain the astrophysics of galaxies.

Key words: galaxies: high-redshift – intergalactic medium – dark ages, reionization, first stars – diffuse radiation – early Universe – cosmology: theory.

1 INTRODUCTION

The Epoch of Reionization (EoR) corresponds to the final major baryonic phase change of the Universe. This occurs when the once cold, neutral hydrogen that permeated the early Universe following recombination is ionized by the cumulative ionizing radiation from astrophysical sources (e.g. stars and galaxies). Observing this phase transition is vitally important, as it reveals insights into the nature, growth, and structure of the first astrophysical sources. These properties can be indirectly inferred through the imprint of their radiation on the intergalactic medium (IGM).

The ubiquity of neutral hydrogen in the early Universe should allow us to detect the imprint of the EoR through the 21-cm hyperfine transition (see e.g. Furlanetto, Oh & Briggs 2006; Morales & Wyithe 2010; Pritchard & Loeb 2012; Zaroubi 2013; Barkana 2016). This 21-cm signal is sensitive both to the thermal and ionization state of the neutral hydrogen in the IGM. Further, being a line transition, the spatial and frequency (redshift) dependence of the 21-cm signal will reveal a full three dimensional (3D) picture of the IGM. Detecting this 21-cm radiation will enable the inference of both the ultra-violet (UV) and X-ray properties of the sources responsible for reionization and the heating of the IGM.

★ E-mail: greigb@unimelb.edu.au

Unfortunately, the cosmic 21-cm signal is extremely faint, buried beneath astrophysical foregrounds which can be up to five orders of magnitude brighter. However, this has not deterred numerous observational efforts to measure this elusive signal. Broadly speaking, these can be separated into two classes of experiments: (i) large-scale interferometer experiments designed to measure the spatial fluctuations in the cosmic 21-cm signal and (ii) global signal experiments which average the signal over the entire visible sky.

Several large-scale radio interferometers have been constructed or proposed. The first generation of these experiments, the Low-Frequency Array (LOFAR; van Haarlem et al. 2013), the Murchison Wide Field Array (MWA; Tingay et al. 2013; Wayth et al. 2018), the Precision Array for Probing the EoR (PAPER; Parsons et al. 2010), the Owens Valley Radio Observatory Long Wavelength Array (OVRO-LWA; Eastwood et al. 2019), and the upgraded Giant Metrewave Radio Telescope (uGMRT; Gupta et al. 2017) have limited sensitivities, requiring several years of observing time to potentially make a low signal-to-noise statistical detection of the signal. Second generation experiments, with considerably higher expected sensitivities, such as the Hydrogen Epoch of Reionization Array (HERA; DeBoer et al. 2017), NenuFAR (New extension in Nançay Upgrading loFAR; Zarka et al. 2012), and the Square Kilometre Array (SKA; Mellema et al. 2013; Koopmans et al. 2015) should be able to provide higher signal-to-noise statistical detections across multiple redshifts. Further, the SKA has been designed to be able to provide the first 3D tomographic images of the EoR.

Somewhat easier to design and operate, there have also been numerous global experiments. These include, the Experiment to Detect the Global EoR Signature (EDGES; Bowman & Rogers 2010), the Sonda Cosmológica de las Islas para la Detección de Hidrógeno Neutro (SCI-HI; Voytek et al. 2014), the Shaped Antenna measurement of the background RAdio Spectrum (SARAS; Patra et al. 2015), Broadband Instrument for Global HydrOgen ReioNisation Signal (BIGHORNS; Sokolowski et al. 2015), the Large Aperture Experiment to detect the Dark Ages (LEDA; Greenhill & Bernardi 2012; Bernardi et al. 2016), Probing Radio Intensity at high-Z from Marion (PRI^{Z}M; Philip et al. 2019), Dark Ages Polarimeter PathfindER (DAPPER[1]), Mapper of the IGM Spin Temperature (MIST[2]) and the Netherlands-China Low-Frequency Explorer (NCLE[3]), and Radio Experiment for the Analysis of Cosmic Hydrogen (REACH[4]).

Despite the wealth of experimental efforts to measure the cosmic 21-cm signal from the early Universe, there has only been one claimed detection during the cosmic dawn, with excess absorption near $z \approx 17$ announced by EDGES (Bowman et al. 2018a). However, the cosmological origin of this signal is heavily disputed in the literature (see Draine & Miralda-Escudé 2018; e.g. Hills et al. 2018; Bowman et al. 2018b; Bradley et al. 2019; Singh & Subrahmanyan 2019) and requires confirmation by an independent experiment.

All other observational efforts to detect the cosmic 21-cm signal have only produced upper limits on the signal amplitude. For global experiments, these correspond to limits on the overall sky-averaged brightness temperature, with best available limits from LEDA (Bernardi et al. 2016), EDGES high-band (Monsalve et al. 2017), and SARAS2 (Singh et al. 2017). Here, we are specifically interested in 21-cm power spectrum (PS) upper limits, as this is a more information rich statistic.

The first 21-cm PS upper limits were measured by the Giant Metrewave Radio Telescope (GMRT; Paciga et al. 2013) at $z \approx 8.6$. Since then, each of the first generation of radio interferometers have all reported upper limits on the 21-cm PS. For LOFAR, these include single-night observations at $z = 9.6-10.6$ (Patil et al. 2017) and more recently, upper limits at $z = 19.8-25.2$ targeting the dark ages and cosmic dawn with the LOFAR-Low Band Antenna array (Gehlot et al. 2019). Recently, the completed PAPER experiment revised their best upper limits (Cheng et al. 2018; Kolopanis et al. 2019) across $z \approx 7.5-11$ following identification of issues in dealing with signal loss from earlier reported limits (Ali et al. 2015). Finally, the MWA recently reported their best upper limits at $z = 6.5-8.7$ from four seasons of observations (Trott et al. 2020), improving on previous measurements in the literature (Dillon et al. 2015; Beardsley et al. 2016; Barry et al. 2019; Li et al. 2019). Other existing upper limits have been obtained at $z \approx 18.4$ by the OVRO-LWA (Eastwood et al. 2019) and at $z = 17.9-18.6$ by the Amsterdam-ASTRON Radio Transients Facility And Analysis Centre (AARTFAAC) Cosmic Explorer (ACE) programme (Gehlot et al. 2020).

With Mertens et al. (2020), LOFAR has now considerably improved their best upper limits on the EoR using 141 h of observations at $z \approx 9.1$ to achieve 21-cm PS 2σ upper limits of $\Delta^2_{21} \approx (73\ \mathrm{mK})^2$ at $k \approx 0.075\,h\,\mathrm{Mpc}^{-1}$. This corresponds to an improvement by a factor of $\approx$8 compared to their previous best upper limit (Patil et al. 2017). While such limits are still several orders of magnitude above fiducial theoretical models (e.g. Mesinger, Greig & Sobacchi 2016), they are aggressive enough to begin to rule out extreme models of reionization known as 'cold' reionization (e.g. Mesinger, Ewall-Wice & Hewitt 2014; Parsons et al. 2014). Here, 'cold' reionization refers to models in which the IGM undergoes little to no heating, adiabatically cooling faster than the cosmic microwave background (CMB) as the Universe expands. This can result in large contrasts between the ionized and neutral IGM, driving 21-cm PS amplitudes in excess of $\Delta^2_{21} \gtrsim 10^4\ \mathrm{mK}^2$. Attempts to rule out such extreme regions of astrophysical parameter space have already been explored for EDGES high-band (Monsalve et al. 2017, 2018, 2019) and the now retracted upper limits from PAPER (Pober et al. 2015; Greig, Mesinger & Pober 2016).

Related studies using these new LOFAR upper limits have already been performed by Ghara et al. (2020) and Mondal et al. (2020). Ghara et al. (2020) focused their analysis on general IGM properties, such as the mean IGM neutral fraction and spin temperature, using GRIZZLY (Ghara, Choudhury & Datta 2015; Ghara et al. 2018). Mondal et al. (2020) perform a similar analysis while also exploring the contribution to the excess radio background from the high-z Universe. For Ghara et al. (2020), their results were obtained from a Monte Carlo Markov Chain (MCMC) trained on 21-cm PS emulators and emulators connecting the source properties to the IGM properties. In Mondal et al. (2020), their results are derived by calculating their likelihood from a large parameter space grid of models populated by a trained emulator. Here, we employ a galaxy model (Park et al. 2019) which allows us to directly compare those models disfavoured by LOFAR against existing observations of ultra-violet (UV) luminosity functions (LFs),[5] as well as other observations of the first billion years. Thus, we place the recent LOFAR upper limits into context with other observational probes,

[1] https://www.colorado.edu/project/dark-ages-polarimeter-pathfinder/
[2] http://www.physics.mcgill.ca/mist/
[3] https://www.isispace.nl/projects/ncle-the-netherlands-china-low-frequency-explorer/
[4] https://www.kicc.cam.ac.uk/projects/reach

[5] For a similar approach connecting the global 21-cm signal to observed UV LFs (see Mirocha, Furlanetto & Sun 2017)

finding that all models currently excluded by these new 21-cm upper limits are also excluded by existing probes, thereby strengthening each others individual evidence and solidly excluding extremely cold IGM models. Our framework directly forward models the 3D 21-cm signal. Thus the inferred, marginalized IGM properties can serve as tests of emulator-based MCMCs, as well as confirming the robustness of the conclusions to the choice of simulation tool.

The outline of the remainder of this paper is as follows. In Section 2, we summarize the details of the astrophysical parametrization used in this analysis, as well as the 21CMMC setup. In Section 3, we discuss the main results and in Section 4, we provide our conclusions. Unless otherwise noted, all quoted quantities are in co-moving units with the following adopted cosmological parameters: $(\Omega_\Lambda, \Omega_M, \Omega_b, n, \sigma_8, H_0) = (0.69, 0.31, 0.048, 0.97, 0.81, 68\,\mathrm{km\,s^{-1}\,Mpc^{-1}})$, consistent with recent results from the Planck mission (Planck Collaboration XIII 2016).

2 METHODOLOGY

2.1 Simulating the 21-cm signal

We use the seminumerical simulation code 21CMFAST[6](Mesinger & Furlanetto 2007; Mesinger, Furlanetto & Cen 2011) to model the cosmic 21-cm signal. In particular, we use the Park et al. (2019) astrophysical parametrization, which adds a host dark matter halo mass dependence to the star-formation rate and ionizing escape fraction. Using simple conversion, this enables 21CMFAST to compute UV LFs for direct comparison against observations of high-z galaxy LFs.

It is important to note that this parametrization is a simplification of the true underlying astrophysics describing the ionizing sources. It assumes only a single population of ionizing sources (i.e. a single power-law relation with halo mass) and ignores any explicit redshift dependence on the escape fraction or stellar mass. Therefore, any conclusions drawn from this work are specific to the assumptions used in this source modelling. However, for the bulk of the galaxy population (i.e. with UV magnitude, $M_{UV} > -20$) the simple Park et al. (2019) parametrization is consistent with both observations of high-z LFs as well as semi-analytical galaxy formation models and hydrodynamical simulations (e.g. Harikane et al. 2016; Mutch et al. 2016; Xu et al. 2016; Tacchella et al. 2018; Behroozi et al. 2019; Yung et al. 2019; Gillet et al., in preparation). As such, there is currently no evidence that a more complicated source model is required at this stage. If more complex modelling is required, these existing parameters can be treated as effective, population averaged quantities. In the future, we can increase the source model complexity and use Bayesian evidence from our forward-modelling approach to quantify whether redshift-dependence is required by the observational data.

Finally, we adopt the on-the-fly ionizing photon non-conservation correction (Park et al., in preparation) which accounts for the fact that the excursion-set formalism used for tracking ionizations is not photon conserving in three dimensions (e.g. McQuinn et al. 2005; Zahn et al. 2007; Paranjape & Choudhury 2014; Paranjape, Choudhury & Padmanabhan 2016; Hassan et al. 2017; Choudhury & Paranjape 2018; Hutter 2018; Molaro et al. 2019). Below, we summarize the main components of 21CMFAST, including the astrophysical parameters, and refer the reader to the aforementioned publications for further information.

[6]https://github.com/andreimesinger/21cmFAST

2.1.1 UV properties of the galaxies

The Park et al. (2019) galaxy parametrization adopts the common assumption that a galaxy's stellar mass, M_*, is proportional to its host halo mass, M_h (e.g. Kuhlen & Faucher-Giguère 2012; Dayal et al. 2014; Behroozi & Silk 2015; Mitra, Choudhury & Ferrara 2015; Mutch et al. 2016; Sun & Furlanetto 2016; Yue, Ferrara & Xu 2016; Hutter et al. 2020). This relationship is modelled as a power-law[7] normalized at $M_h = 10^{10}\,M_\odot$:

$$M_*(M_h) = f_* \left(\frac{\Omega_b}{\Omega_M}\right) M_h, \tag{1}$$

and

$$f_* = f_{*,10} \left(\frac{M_h}{10^{10}\,M_\odot}\right)^{\alpha_*}, \tag{2}$$

with f_* being the fraction of galactic gas in stars, $f_{*,10}$ its normalization, and α_* the power-law index.

This stellar mass can then be divided by a characteristic time-scale to estimate a galaxy's star-formation rate (SFR), $\dot{M}_*$,

$$\dot{M}_*(M_h, z) = \frac{M_*}{t_* H^{-1}(z)}, \tag{3}$$

where t_* is a unit less quantity freely allowed to vary between zero and unity and $H^{-1}(z)$ is the Hubble time.

Equivalently, the UV ionizing escape fraction, f_{esc}, is parametrized to be a power-law dependent on halo mass,

$$f_{esc} = f_{esc,10} \left(\frac{M_h}{10^{10}\,M_\odot}\right)^{\alpha_{esc}}, \tag{4}$$

with $f_{esc,10}$ again normalized at a halo of mass $10^{10}\,M_\odot$ with the power-law index, α_{esc}. Note that for both f_* and f_{esc}, we impose a physical upper limit of unity (i.e. $f_* \leq 1$ and $f_{esc} \leq 1$).

Finally, not all small mass haloes are capable of hosting active, star-forming galaxies owing to inefficient cooling and/or feedback processes. In order to mimic this process, a duty-cycle is included to suppress their contribution

$$f_{duty} = \exp\left(-\frac{M_{turn}}{M_h}\right). \tag{5}$$

In effect, some fraction, $(1 - f_{duty})$, of dark matter haloes with mass M_h are prevented from hosting star-forming galaxies, with the characteristic scale for this suppression being set by M_{turn} (e.g. Giroux, Sutherland & Shull 1994; Shapiro, Giroux & Babul 1994; Hui & Gnedin 1997; Barkana & Loeb 2001; Springel & Hernquist 2003; Mesinger & Dijkstra 2008; Okamoto, Gao & Theuns 2008; Sobacchi & Mesinger 2013a,b)

In summary, this results in six free parameters describing the UV galaxy properties in our model, $f_{*,10}, f_{esc,10}, \alpha_*, \alpha_{esc}, M_{turn}$, and t_*.

2.1.2 X-ray properties of the galaxies

Prior to reionization, it is thought that the IGM undergoes heating in the early Universe due to X-rays. The likely, dominant source of these X-rays are stellar remnants within the first galaxies. In 21CMFAST, X-ray heating is calculated through the angle-averaged specific X-ray intensity, $J(\boldsymbol{x}, E, z)$, (in $\mathrm{erg\,s^{-1}\,keV^{-1}\,cm^{-2}\,sr^{-1}}$). This is estimated

[7]At $z \gtrsim 5$, this power-law dependence is recovered both by the population averaged relation obtained from semi-analytic models (e.g Mutch et al. 2016; Yung et al. 2019; Hutter et al. 2020) and semi-empirical fits to observations (e.g. Harikane et al. 2016; Tacchella et al. 2018; Behroozi et al. 2019).

by integrating the co-moving X-ray specific emissivity, $\epsilon_X(\boldsymbol{x}, E_e, z')$, evaluated in the emitted frame, $E_e = E(1+z')/(1+z)$, back along the light-cone:

$$J(\boldsymbol{x}, E, z) = \frac{(1+z)^3}{4\pi}\int_z^\infty \mathrm{d}z' \frac{c\mathrm{d}t}{\mathrm{d}z'}\epsilon_X e^{-\tau}, \quad (6)$$

where the probability of attenuation by the IGM is accounted for through its optical depth, $e^{-\tau}$. The co-moving specific emissivity is then,

$$\epsilon_X(\boldsymbol{x}, E_e, z') = \frac{L_X}{\mathrm{SFR}}\left[(1+\bar{\delta}_{nl})\int_0^\infty \mathrm{d}M_h \frac{\mathrm{d}n}{\mathrm{d}M_h} f_{duty}\dot{M}_*\right], \quad (7)$$

where $\bar{\delta}_{nl}$ is the non-linear density averaged over a shell centred on $(\boldsymbol{x}, z)$ and the expression in square brackets corresponds to the SFR density along the light-cone.

The co-moving emissivity, as defined above in equation (7), is normalized by the specific X-ray luminosity per unit star formation escaping the host galaxies, L_X/SFR ($\mathrm{erg\,s^{-1}\,keV^{-1}\,M_\odot^{-1}\,yr}$). It is modelled as a power-law, $L_X \propto E^{-\alpha_X}$, which is attenuated below a threshold energy, E_0, describing the absorption of lower energy X-ray photons by the host galaxy. The specific luminosity is then converted to an integrated soft-band (<2 keV) luminosity per SFR, $L_{X<2\,\mathrm{keV}}/\mathrm{SFR}$ ($\mathrm{erg\,s^{-1}\,M_\odot^{-1}\,yr}$), which is a free parameter in the model

$$L_{X<2\,\mathrm{keV}}/\mathrm{SFR} = \int_{E_0}^{2\,\mathrm{keV}} \mathrm{d}E_e\; L_X/\mathrm{SFR}. \quad (8)$$

This 2 keV limit equates to an X-ray mean-free path of the order of the Hubble length at high-z, thus X-ray photons harder that this limit will not contribute to heating the IGM (e.g. McQuinn 2012).

In summary, we have three free parameters describing the X-ray properties, $L_{X<2\,\mathrm{keV}}/\mathrm{SFR}$, E_0, and α_X.

2.1.3 Ionization and thermal state of the IGM

In 21CMFAST, the evolved density and velocity fields are obtained following second-order Lagrange perturbation theory (e.g Scoccimarro 1998). Reionization is then determined at each redshift from this evolved density field by tracking the balance between the total number of ionizing photons against the number of neutral hydrogen atoms plus total recombinations in spheres of decreasing radii. A cell is considered as ionized when the total number of ionizing photons released per baryon, n_{ion} exceeds the total number of recombinations, $\bar{n}_{rec}$ (e.g. Sobacchi & Mesinger 2014)

$$n_{ion}(\boldsymbol{x}, z|R, \delta_R) \geq (1+\bar{n}_{rec})(1-\bar{x}_e). \quad (9)$$

n_{ion}, calculated within a spherical region of size, R, and smoothed overdensity, δ_R, is given by,

$$n_{ion} = \bar{\rho}_b^{-1}\int_0^\infty \mathrm{d}M_h \frac{\mathrm{d}n(M_h, z|R, \delta_R)}{\mathrm{d}M_h} f_{duty}\dot{M}_* f_{esc} N_{\gamma/b}, \quad (10)$$

where $\bar{\rho}_b$ is the mean baryon density, $\frac{\mathrm{d}n}{\mathrm{d}M_h}$ is the conditional halo mass function (HMF), which is the Press-Schecter HMF (Lacey & Cole 1993) normalized to the mean of the Sheth–Tormen HMF (Sheth & Tormen 1999), and $N_{\gamma/b}$ is the number of ionizing photons per stellar baryon.[8]The last term in equation (9), $(1-\bar{x}_e)$, accounts for ionizations by X-rays, which are estimated to contribute only around ∼10–15 per cent of total ionizations (e.g. Ricotti & Ostriker 2004; Mesinger, Ferrara & Spiegel 2013; Madau & Fragos 2017; Ross et al. 2017; Eide et al. 2018).

The thermal state of the neutral IGM (and its partial ionizations) are obtained by self-consistently calculating the adiabatic and Compton heating and cooling rates, heating following partial ionizations as well X-ray heating and ionizations (as discussed above). Finally, the IGM spin temperature, T_S, is estimated as a weighted mean of the gas and CMB temperatures, dependent on the local gas density and the intensity of the Lyman-α (Ly α) radiation imparted on the simulation cell (Wouthuysen 1952; Field 1958).

This Ly α background is produced by the summed contribution from two components. First, the X-ray excitations of neutral hydrogen atoms ($J_{\alpha,X}$), which is set by the X-ray heating rate assuming a balance between energy injection and redshifting of photons out of Ly α resonance (Pritchard & Furlanetto 2007). The second, the direct stellar[9] emission of Lyman band photons by the first sources, whereby any IGM absorbed Lyman-n resonance photon will cascade with a recycling fraction through Ly α resulting in a background, $J_{\alpha,*}$, that is the cumulative sum over all Lyman resonances (e.g. Barkana & Loeb 2005). For further details, see Mesinger et al. 2011.

2.1.4 Ionizing photon non-conservation correction

As 21CMFAST employes an excursion-set formalism for determining which cells are ionized, it is impacted by the resultant non-conservation of ionizing photons. This arises within cells that exceed the ionization criteria (equation 9), where the excess ionizing photons that are left over after ionizing the neutral hydrogen are not propagated onwards. This behaviour acts as an effective bias on the ionizing escape fraction, f_{esc}. Roughly speaking, this corresponds to a loss of ∼10–20 per cent of the ionizing photons (e.g. McQuinn et al. 2005; Zahn et al. 2007; Paranjape & Choudhury 2014; Paranjape et al. 2016; Hassan et al. 2017; Choudhury & Paranjape 2018; Hutter 2018; Molaro et al. 2019).

Both Choudhury & Paranjape (2018) and Molaro et al. (2019) have introduced new, explicitly photon conserving algorithms for seminumerical simulations. While being orders of magnitude faster than full radiative-transfer simulations, they are still considerably slower than conventional seminumerical simulations. Under Bayesian parameter estimation approaches such as 21CMMC, these schemes are still intractable when forward modelling the 21-cm signal in the high-dimensional parameter spaces required to characterize the ionizing, soft UV, and X-ray properties of the first galaxies.

Instead, Park et al., in preparation, introduce an approximate correction to the ionizing photon non-conservation issue, correcting for the effective bias on f_{esc} by analytically solving for the correct evolution of the ionization fraction for a given source model, under the assumption of no correlations between the sources and sinks (which should only impact the final ∼10 per cent of the EoR; Sobacchi & Mesinger 2014).

This analytic solution is compared against a calibration curve from 21CMFAST considering only ionizations (i.e. no recombinations or spin temperature evolution). If photons were conserved, these two curves would be identical. However, in practice, the 21CMFAST history is delayed due to the loss of ionizing photons. In order to

[8]The default value in 21CMFAST is chosen to be 5000, which corresponds to a Salpeter initial mass function (Salpeter 1955). Note though that $N_{\gamma/b}$ is strongly degenerate with f_*.

[9]Note, currently the UV spectra for the stellar emission component is held fixed and does not consider any other potential source of soft UV photons, such as quasars (see e.g. Qin et al. 2017; Ricci et al. 2017; Mitra, Choudhury & Ferrara 2018).

recalibrate 21CMFAST, we decrease the redshift used for determining the ionization field.[10] Note, this modified redshift is only used for modifying the ionization field, all other quantities are calculated at the original redshift. We find that for the bulk of the EoR, this corresponds roughly to a shift in redshift of $\Delta z \sim 0.3 \pm 0.1$.

2.1.5 *Computing the 21-cm signal*

Combining all the cosmological fields discussed in the previous section, we compute the observable cosmic 21-cm signal as a brightness temperature contrast relative to the CMB temperature, $T_{\rm CMB}$ (e.g. Furlanetto et al. 2006)

$$\delta T_{\rm b}(\nu) = \frac{T_{\rm S} - T_{\rm CMB}(z)}{1+z}\left(1 - {\rm e}^{-\tau_{\nu_0}}\right)\ {\rm mK}, \tag{11}$$

where τ_{ν_0} is the optical depth of the 21-cm line

$$\tau_{\nu_0} \propto (1+\delta_{\rm nl})(1+z)^{3/2}\frac{x_{\rm H\,I}}{T_{\rm S}}\left(\frac{H}{{\rm d}v_{\rm r}/{\rm d}r + H}\right). \tag{12}$$

Here, $\delta_{\rm nl} \equiv \rho/\bar{\rho} - 1$ is the gas overdensity, $x_{\rm H\,I}$ is the neutral hydrogen fraction, $T_{\rm S}$ is the gas spin temperature, $H(z)$ is the Hubble parameter, and ${\rm d}v_{\rm r}/{\rm d}r$ is the velocity gradient along the line of sight. Above, we have dropped the spatial dependence for brevity and all quantities are evaluated at redshift $z = \nu_0/\nu - 1$, where ν_0 is the 21-cm frequency. Finally, we include line-of-sight redshift space distortions through the approach outlined in Mao et al. (2012), Jensen et al. (2013), and Greig & Mesinger (2018).

2.2 Astrophysical parameter set

In total, there are nine free astrophysical parameters to describe the adopted astrophysical model. Below, we summarize each of these and the associated parameter ranges we adopt based on previous explorations with 21CMMC (Greig et al. 2017; Park et al. 2019). We additionally summarize these in the top row of Table 1. Within 21CMMC, we adopt flat priors over all of these parameter ranges.

(i) $f_{*,\,10}$: the normalization factor, evaluated at a halo mass of $10^{10}\,{\rm M}_{\odot}$, for the fraction of galactic gas in stars power law with halo mass. This is allowed to vary in the log as, $\log_{10}(f_{*,\,10}) \in [-3, 0]$. At high redshift, estimates of $f_{*,\,10}$ obtained from either observations or simulations are highly uncertain with large scatter (e.g. Wise et al. 2014; Behroozi & Silk 2015; Sun & Furlanetto 2016; Xu et al. 2016), thus we consider a broad range to encompass the uncertainty.

(ii) α_*: the power-law index for the star formation as a function of halo mass, allowed to vary between, $\alpha_* \in [-0.5, 1]$. This power-law index is driven by stellar feedback processes, which can be driven by a broad range of physical processes (see, for example, discussions in Mirocha 2019, 2020). For example, at 68 per cent confidence, Park et al. (2019) recover constraints of $\alpha_* = 0.50^{+0.07}_{-0.06}$ from existing *Hubble* Space Telescope UV LFs. Thus, this range is conservatively selected to account for unseen galaxies whose properties may differ from the observed ones.

(iii) $f_{\rm esc,\,10}$: the normalization factor, evaluated at a halo mass of $10^{10}\,{\rm M}_{\odot}$, for the ionizing UV escape fraction power law with halo mass. We vary this in the log range, $\log_{10}(f_{\rm esc,\,10}) \in [-3, 0]$. As for $f_{*,\,10}$, estimates of $f_{\rm esc,\,10}$ at high redshift are highly uncertain with large scatter (e.g. Kimm & Cen 2014; Paardekooper, Khochfar & Vecchia 2015; Xu et al. 2016; Kimm et al. 2017; Ma et al. 2020). Thus again, we consider a broad range to account for the uncertainty.

(iv) $\alpha_{\rm esc}$: the power-law index for the ionizing UV escape fraction as a function of halo mass, allowed to vary in the range, $\alpha_{\rm esc} \in [-1, 0.5]$. This range encompasses the broad range in values estimated from both analytic approaches applied to UV luminosity functions (e.g. Mason, Trenti & Treu 2015; Mutch et al. 2016; Sun & Furlanetto 2016) as well as hydrodynamical simulations (e.g Gnedin & Kaurov 2014; Paardekooper et al. 2015; Ocvirk et al. 2016; Xu et al. 2016; Kimm et al. 2017; Katz et al. 2018; Ma et al. 2020). In fact, most hydrodynamical simulations predict an increasing $f_{\rm esc}$ with decreasing halo mass (i.e. $\alpha_{\rm esc} < 0$). However, Ma et al. (2020) predict a fairly constant or slightly decreasing $f_{\rm esc}$ with decreasing halo mass (i.e. $\alpha_{\rm esc} > 0$). Thus, we have conservatively included a broad range skewed towards negative $\alpha_{\rm esc}$.

(v) t_*: the star formation time-scale as a fraction of the Hubble time, allowed to vary in the range, $t_* \in (0, 1]$.

(vi) $M_{\rm turn}$: the characteristic halo mass turn-over scale below which the number density of active star-forming galaxies are exponentially suppressed by the adopted duty cycle. This is allowed to vary within the range, $\log_{10}(M_{\rm turn}) \in [8, 10]$. This lower limit is motivated by the atomic cooling threshold for haloes, whereas the upper limit is consistent with estimates of host halo masses obtained via abundance matching from observed Lyman break galaxies at $z \sim 6 - 8$ (e.g. Kuhlen & Faucher-Giguère 2012; Barone-Nugent et al. 2014).

(vii) E_0: the minimum energy threshold for X-ray photons to escape their host galaxy. Allowed to vary within the range, $E_0 \in [0.2, 1.5]\,{\rm keV}$, which corresponds of an integrated column density of, $\log_{10}(N_{\rm H\,I}/{\rm cm}^2) \in [19.3, 23.0]$. The lower limit is motivated by numerical simulations estimating the impact of attenuation by the host galaxy (e.g. Fragos et al. 2013b; Das et al. 2017) whereas the upper limit roughly corresponds to photons with a mean free path that exceeds the Hubble length at the redshifts of interest; thus X-ray photons with higher energies would not interact with the IGM.

(viii) $L_{\rm X<2\,keV}/{\rm SFR}$: the soft-band ($E_0 - 2\,{\rm keV}$) X-ray luminosity per unit star formation normalization. Allowed to vary across, $\log_{10}(L_{\rm X<2\,keV}/{\rm SFR}) \in [30, 42]$. Here, we considerably reduce the lower bound for $L_{\rm X<2\,keV}/{\rm SFR}$ compared to what is typically chosen (i.e. Park et al. 2019) in order to explore truly 'cold' reionization scenarios. This upper limit is one to two orders of magnitude larger than observed in local star-forming galaxies, which allows for an increased X-ray luminosity due to, for example, more luminous X-ray binaries in low-metallicity environments, such as those expected within the first galaxies (Basu-Zych et al. 2013; Fragos et al. 2013a; Brorby, Kaaret & Prestwich 2014; Douna et al. 2015; Brorby et al. 2016; Lehmer et al. 2016).

(ix) $\alpha_{\rm X}$: the power-law index for the SED of X-ray sources, which we allow to vary between $\alpha_{\rm X} \in [-1, 3]$. This choice covers a wide variety of plausible X-ray SEDs, for example, high-mass X-ray binaries, mini-quasars, supernovae remnants, the host interstellar medium etc. (see McQuinn 2012; Pacucci et al. 2014 for further details).

2.3 21CMMC setup

21CMMC [11](Greig & Mesinger 2015, 2017; Greig & Mesinger 2018; Park et al. 2019) is the massively parallel, publicly available MCMC sampler of the 3D seminumerical reionization simulations code 21CMFAST. It uses the existing PYTHON modules COSMOHAMMER

[10]This effectively amounts to boosting the number of ionizations to compensate for the ionizing photon non-conservation. However, we do not know a priori how much to boost ionizations by, thus, we modify the redshift to allow our calculation to be performed on-the-fly.

[11]https://github.com/BradGreig/21CMMC

Table 1. Summary of the 68th and 95th percentile limits on the disfavoured regions of nine astrophysical parameters included in 21CMMC using the LOFAR upper limits at $z \approx 9.1$ from Mertens et al. (2020).

	$\log_{10}(f_{*,10})$	α_*	$\log_{10}(f_{\rm esc,10})$	$\alpha_{\rm esc}$	$\log_{10}(M_{\rm turn})$ [$M_\odot$]	t_*	$\log_{10}\left(\frac{L_{X<2keV}}{SFR}\right)$ [erg s^{-1} $M_\odot^{-1}$ yr]	E_0 [keV]	α_X
Prior ranges	[−3.0, 0.0]	[−0.5,1.0]	[−3.0, 0.0]	[−1.0,0.5]	[8.0,10.0]	(0.0,1.0]	[30.0,42.0]	[0.2,1.5]	[−1.0,3.0]
68th percentile limits	[−1.06,0.0]	[0.28,1.0]	[−1.27, −0.39]	[−0.11, 0.5]	[8.66, 10.0]	[0.0, 0.76]	[30, 36.58]	[0.2,1.5]	[−0.2, 3.0]
95th percentile limits	[−1.53,0,0]	[−0.23,1.0]	[−1.64, 0.0]	[−0.64, 0.5]	[8.13, 10.0]	[0.0, 0.96]	[30, 39.04]	[0.2,1.5]	[−0.87, 3.0]

(Akeret et al. 2013), and EMCEE (Foreman-Mackey et al. 2013), an affine invariant ensemble sampler from Goodman & Weare (2010). For each new proposal step within the MCMC, 21CMMC performs a fully independent 3D realization of the 21-cm signal.

Typically, we would perform our MCMC seeking to maximize the likelihood that our astrophysical model is consistent with the observational data. However, current upper limits on the 21-cm signal are not strong enough to yield statistically significant constraints on the astrophysical parameter space. Instead, following Ghara et al. (2020), we invert the typical problem by reversing the likelihood, maximizing models which exceed the observational limits.[12] This enables us to explore the regions of astrophysical parameter space inconsistent with the recent LOFAR upper limits at $z \approx 9.1$.

In this work, we model the likelihood as a one-sided Gaussian. This differs from the likelihood adopted by Ghara et al. (2020) and Mondal et al. (2020). The primary difference stems from the interpretation of the observational limits obtained by Mertens et al. (2020), where the upper limits are reported as data points with error bars. Following this interpretation, Ghara et al. (2020) and Mondal et al. (2020) construct their likelihood using an error function centred on the data points (see e.g. Appendix A in Ghara et al. 2020). Alternatively, we treat the upper limits as true limits (rather than data points), as limits should be consistent with zero. Ultimately, both approaches are similar as they equally assume that the uncertainty on the power spectrum measurements are drawn from a normal distribution. The only difference is that our likelihood is offset to higher power spectrum values, as it is only non-zero beyond the upper-limit, resulting in it being more conservative than that used by Ghara et al. (2020) and Mondal et al. (2020). In order to verify that our adopted likelihood function does not bias our results, we have post-processed our existing data using the likelihood used by Ghara et al. (2020) and Mondal et al. (2020). We find negligible differences between the marginalized posteriors using the two different likelihood functions.

Our likelihood, $\mathcal{L}$, for models disfavoured by LOFAR is then given by,[13]

$$\mathcal{L} = \begin{cases} 0 & \Delta^2_{21,m} < \Delta^2_{21,d} \\ 1 - \exp\left[-\frac{1}{2}\left(\frac{\Delta^2_{21,m} - \Delta^2_{21,d}}{\sigma_i}\right)^2\right] & \Delta^2_{21,m} \geq \Delta^2_{21,d}, \end{cases} \quad (13)$$

where $\Delta^2_{21,m}$ and $\Delta^2_{21,d}$ correspond to the 21-cm PS from the astrophysical model sampled in 21CMMC and the LOFAR upper limits, respectively.[14] Note, we have dropped the Fourier dependence from these terms, i.e. $\Delta^2_{21,m} = \Delta^2_{21,m}(k_i)$, for brevity. In this work, we only evaluate the likelihood at a single k (i.e. $k \approx 0.075\,h\,{\rm Mpc}^{-1}$), motivated by the fact that all 21CMFAST models were found to be below the upper limits for all other k-bins. This likelihood is then interpreted as

(i) astrophysical models below the upper limit (i.e. $\Delta^2_{21,m} < \Delta^2_{21,d}$) are perfectly consistent with the LOFAR upper limits and are thus given a likelihood of zero.

(ii) above the upper limit (i.e. $\Delta^2_{21,m} \geq \Delta^2_{21,d}$), the likelihood smoothly transitions from zero following a one-sided Gaussian of width equal to the total uncertainty, σ, on the upper limit measurement. This implies astrophysical models with amplitudes much larger than the limit are ruled-out with greater certainty than those close to the central-limit.

The total uncertainty, σ on the upper limit is the quadrature sum of the quoted uncertainty on the limit value from Mertens et al. (2020) and a conservative 20 per cent multiplicative modelling uncertainty on the sampled 21-cm PS obtained from 21CMMC. This modelling uncertainty is motivated by the adopted approximations used in seminumerical simulations, and whose amplitude is estimated relative to radiative-transfer simulations (e.g. Zahn et al. 2011; Ghara et al. 2018; Hutter 2018).

The largest scale probed by the LOFAR upper limits corresponds to $k \approx 0.075\,h\,{\rm Mpc}^{-1}$, which is a factor of 2 larger than the typical sampling scale adopted in 21CMMC (i.e. $k = 0.1-1.0\,{\rm Mpc}^{-1}$). Therefore, to adequately sample these much larger spatial scales, within 21CMMC, we perform 3D realizations of the cosmic 21-cm signal in a box of 400 Mpc and 128 voxels per side-length.[15] This corresponds to a resolution that is ∼3 Mpc per voxel, slightly larger than the preferred resolution of 21CMFAST. However, we have performed convergence tests to verify that the increased resolution of ∼3 Mpc per voxel does not alter the results.

3 RESULTS

3.1 Disfavoured parameters

In Fig. 1, we present the marginalized one and two dimensional posterior distributions recovered from the full output from 21CMMC

[12]This approach corresponds to identifying models ruled out by LOFAR in order to allow our forward modelling approach to converge quicker.

[13]This choice of zero is motivated by the fact that we model our likelihood as a one-sided Gaussian. Any model below the upper limit is perfectly consistent with the data, and thus would normally have a likelihood of unity. However, since we are interested in models which instead exceed the upper limits, we then subtract by unity resulting in zero likelihood.

[14]This assumes the sample variance error is Gaussian distributed, which is a reasonable approximation in the modest S/N regime relevant for current and upcoming observations (Mondal, Bharadwaj & Majumdar 2017; Shaw, Bharadwaj & Mondal 2020). Also, this assumes that the observed data is not correlated across k-bins. Certainly, owing to the non-Gaussian nature of the 21-cm signal this will not be the case in reality, however, at present observations are noise or systematics dominated at levels well above the expected correlations amongst k-bins from the 21-cm signal. Further, in this work, all the constraining power comes from a single k-bin, at $k \approx 0.075\,h\,{\rm Mpc}^{-1}$, thus the impact of this is negligible.

[15]For our simulation volume, we estimate a sample variance of ∼13 per cent for the largest physical scale sampled by LOFAR (i.e. $k \approx 0.075\,h\,{\rm Mpc}^{-1}$), which is well below that of the combined error from the observations and modelling uncertainty.

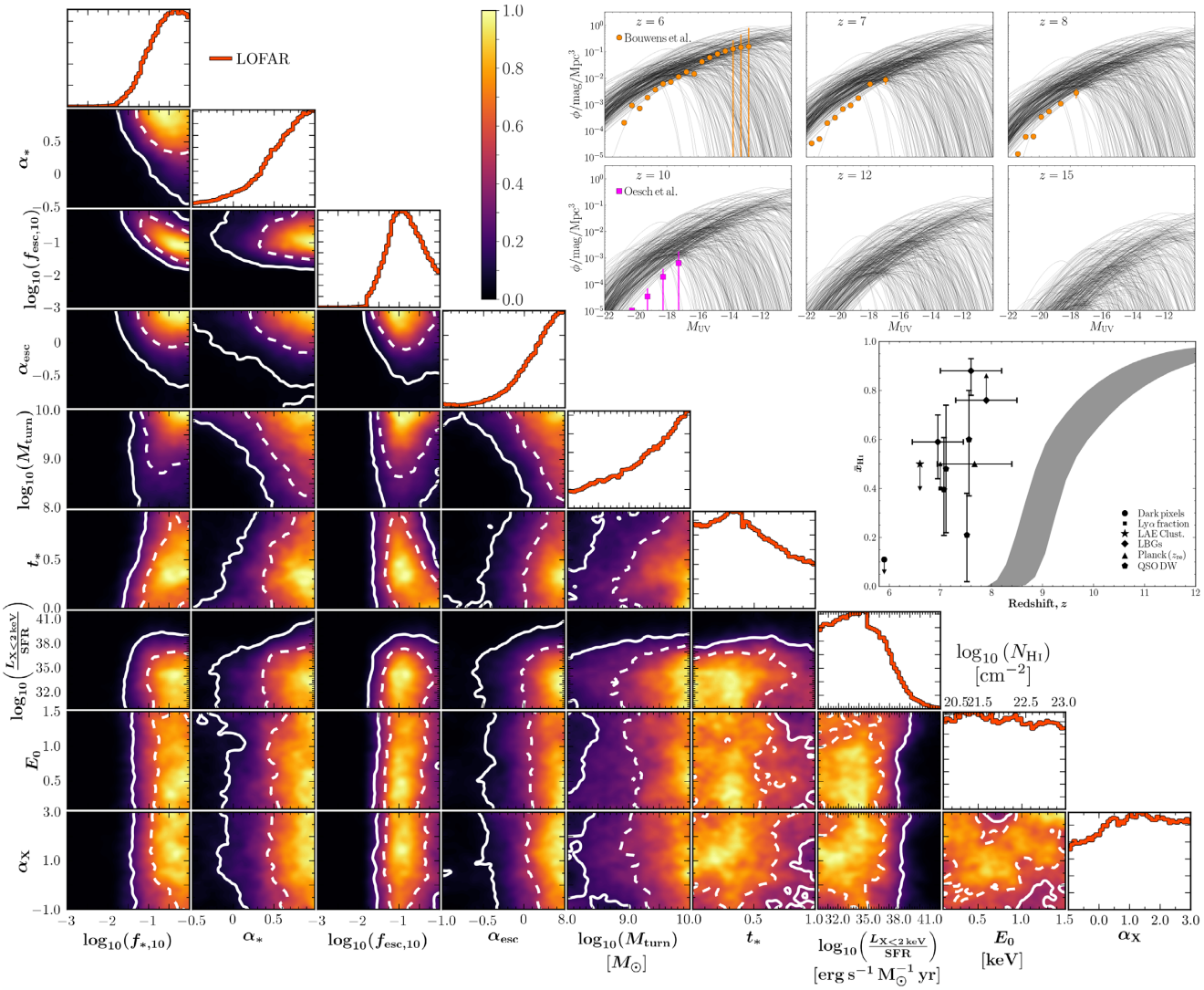

Figure 1. Marginalized one and two dimensional posterior distributions for the parameters which are disfavoured by just the LOFAR upper limits (i.e. no other observational probes) at $z \approx 9.1$ (Mertens et al. 2020). White dashed (solid) contours correspond to the 68th (95th) percentiles. The colour bar corresponds to the marginalized probability (normalized such that the largest marginalized probability is unity for each two dimensional posterior) of the models being disfavoured. In the top right-hand panels, we provide 500 randomly sampled LFs which are drawn from the posterior of models that exceed the LOFAR upper limits and are compared against existing constraints at $z = 6-8$ (Bouwens et al. 2015, 2017) and $z = 10$ (Oesch et al. 2018). In the middle right-hand panel, we compare the bounds on the reionization histories disfavoured by LOFAR to all current observational constraints on the IGM neutral fraction (see text for further details).

using the setup described in Section 2.3 for the nine input parameters outlined in Section 2.2. The colour bar denotes the normalized probably for the models disfavoured by LOFAR, with larger probabilities highlighting regions more strongly disfavoured. Note that these results are obtained using only the LOFAR upper limits, no other existing observational constraints are used. The resultant 68th and 95th percentile limits on these parameters disfavoured by the LOFAR limits are summarized in Table 1. It is immediately evident that this parameter set contains several strong degeneracies, indicating that our relative model complexity is not required by the existing observational data. Instead, the choice to explore the larger astrophysical parameter set is simply a demonstration of the flexible and physically motivated parametrization available with 21CMFAST and 21CMMC, which allows easy comparison against observational constraints such as the high-z UV LFs. It is imperative to point out here that we are only exploring models which exceed the LOFAR upper limits at $z \approx 9.1$, given the full prior ranges outlined in Section 2.2. That is our adopted likelihood only adds non-zero weight to regions within the full astrophysical parameter space that can exceed the LOFAR upper limits. This approach is more of a demonstration that: (i) LOFAR is already capable of ruling out some models and (ii) that forward modelled MCMC tools during the EoR such as 21CMMC are necessary for interpreting the results. Nevertheless, below we discuss some of the deductions that can be made from the existing LOFAR upper limits. Note again though, that these results are specific to the underlying assumptions of our source model.

The most interesting limit that we can discern from Fig. 1 is that of the soft-band X-ray luminosity, $L_{\rm X<2\,keV}/{\rm SFR}$. This directly controls the amount of heating that the IGM undergoes between the dark ages and reionization and is responsible for the 'cold' reionization scenarios. At 95 per cent confidence, we are able to place limits of $\log_{10}(L_{\rm X<2\,keV}/{\rm SFR}) \lesssim 39.04$. These limits sit below those from local populations of star-forming galaxies (Mineo, Gilfanov &

Sunyaev 2012), stacked *Chandra* observations (Lehmer et al. 2016) and predictions at high-redshifts by population synthesis models (Fragos et al. 2013a). For the remaining two galaxy X-ray properties, E_0 and α_X we are currently unable to place any meaningful limits. This is driven by the fact that we are ruling out models with little to no X-ray heating. In the absence of X-ray heating, it does not matter how much the X-ray SED is attenuated or its power-law shape.

For the galaxy UV properties, the limits are driven by the requirement to maximize the 21-cm PS amplitude at $z \approx 9.1$ (to be able to exceed the LOFAR limit). This occurs when we are roughly at the mid-point of reionization (i.e. $\bar{x}_{\rm H\,I} \sim 0.5$) where the 21-cm PS peak is typically[16] at its maximum (e.g. Mellema et al. 2006; Lidz et al. 2008). Therefore, the limits on $f_{*,\,10}$, α_*, $f_{\rm esc,\,10}$, $\alpha_{\rm esc}$, and $M_{\rm turn}$ are completely degenerate. For $f_{\rm esc,\,10}$, we recover constraints on disallowed values, but for the remainder, we only recover limits. This arises due to the completely degenerate nature between $f_{*,\,10}$ and $f_{\rm esc,\,10}$ for single redshift measurements and the absence of any other observational constraints (i.e. UV LFs, Park et al. 2019). Further contributing to this are the different prior ranges for the corresponding power-law indices α_* and $\alpha_{\rm esc}$. Nevertheless, these limits imply that LOFAR disfavours normalizations of the mass dependent star formation rate, $f_{*,\,10}$ and escape fraction, $f_{\rm esc,\,10}$, to be above $\sim$3.1 and $\sim$2.3 per cent, respectively. Also, a minimum source mass above $\log_{10}(M_{\rm turn}) \gtrsim 8.13$ is disfavoured at 95 per cent confidence.

Unfortunately, owing to differences in the choice of varied parameters (and their allowed ranges), their corresponding meaning (i.e. the mass dependence of star formation rates and escape fractions in 21CMFAST), direct comparison to the results of Ghara et al. (2020) is not possible. However, the general trends of both this work and of Ghara et al. (2020) are consistent: (i) EoR to be ongoing at $z \approx 9.1$ disfavouring low mass star-forming galaxies and high ionizing escape fractions, and (ii) very low X-ray luminosities.

Similar is also true for comparisons with Mondal et al. (2020), however, under some crude simplifying assumptions, we are able to make some rough qualitative comparisons. Considering their standard scenario of astrophysical models (i.e. no excess radio background) they have a total of five model parameters, of which only three are roughly comparable. A fourth, the electron scattering optical depth, $\tau_{\rm e}$ is a free parameter in their model, and we compare against our output $\tau_{\rm e}$ in Section 3.2.3.

Firstly, Mondal et al. (2020) considers only a constant f_* and at 68 per cent confidence disfavour $f_* > 0.05$. In contrast, we have a halo-mass dependent f_* (see equation 2), thus it is not a trivial comparison. Further, we are only inferring limits, rather than obtaining constraints, thus it is difficult to collapse our results into a comparable quantity. However, with these caveats in mind, we can crudely compare the normalization, $f_{*,\,10}$, of our power-law expression, for which we recover disfavoured limits of $f_{*,\,10} \gtrsim 0.09$ at 68 per cent confidence. Broadly speaking, under these simplifying assumptions, these are in agreement.

Next, the circular velocities, $V_{\rm c}$, of the dark matter haloes are disfavoured for $V_{\rm c} < 36\,{\rm km\,s^{-1}}$ at 68 per cent confidence by Mondal et al. (2020). At $z = 9.1$, this corresponds to a halo mass of $9.5 \times 10^8\,{\rm M}_\odot$. Under this parametrization, this corresponds to a sharp cut-off in halo-mass for the ionizing sources. However, in 21CMFAST, the contribution of ionizing sources below the characteristic scale, $M_{\rm turn}$, is fractionally suppressed by the duty cycle (equation 5) resulting in a more gradual decline in the ionizing photon contribution compared with this sharp cut-off. In any case, we recover disfavoured limits of $M_{\rm turn} > 4.5 \times 10^8\,{\rm M}_\odot$ at 68 per cent confidence. Due to this duty cycle term, our definition for $M_{\rm turn}$ is expected to be lower than an equivalent sharp cut-off transition. Further, weaker constraints are expected owing to the larger number of free parameters (and associated degeneracies). For example, a lower $M_{\rm turn}$ and an $f_{\rm esc}$ which increases with halo mass would produce a similar reionization history to one with a larger $M_{\rm turn}$ and constant $f_{\rm esc}$ (as assumed in the Mondal et al. 2020 model). Nevertheless, the limits between these two works are broadly consistent.

Finally, Mondal et al. (2020) disfavour $f_X < 5 \times 10^{-3}$ at 68 per cent confidence, which is a normalization constant to their total X-ray luminosity, L_X/SFR. In 21CMFAST, the X-ray luminosity is parametrized in terms of the soft-band luminosity, $L_{\rm X<2\,keV}$/SFR (equation 8). Thus, comparing between works requires assumptions about the threshold energy, E_0 and the X-ray spectral index, α_X. Taking $E_0 = 0.5\,{\rm keV}$ and $\alpha_X = 1.0$, this disfavoured limit for f_X becomes $L_{\rm X<2\,keV}/{\rm SFR} \lesssim 4.5 \times 10^{37}\ {\rm erg\,s^{-1}\,M_\odot^{-1}\,yr}$. In comparison, our disfavoured limit at 68 per cent confidence is $L_{\rm X<2\,keV}/{\rm SFR} \lesssim 3.8 \times 10^{36}\ {\rm erg\,s^{-1}\,M_\odot^{-1}\,yr}$. However, given the limits on $L_{\rm X<2\,keV}/{\rm SFR}$ are obtained after marginalizing over E_0 and α_X (and the galaxy UV parameters) we expect our inferred value to be weaker. Thus under our assumptions, we infer our results to be consistent with those in Mondal et al. (2020).

3.2 Comparison against existing observations

Next, we focus more on globally averaged quantities and how they compare against existing independent observations and limits in the literature.

3.2.1 *Reionization history*

In the middle right-hand panel of Fig. 1, we present a census of all existing constraints on the IGM neutral fraction against the full range of reionization histories disfavoured by LOFAR (shaded region). We compare against the dark pixel statistics of high-z quasars (QSOs; McGreer, Mesinger & D'Odorico 2015), Lyα fraction (Mesinger et al. 2015), the clustering of Lyα emitters (LAEs; Sobacchi & Mesinger 2015), the Lyα equivalent width distribution of Lyman-break galaxies (LBGs; Mason et al. 2018; Hoag et al. 2019; Mason et al. 2019), the neutral IGM damping wing imprint from high-z QSOs (Greig et al. 2017; Davies et al. 2018; Greig, Mesinger & Bañados 2019), and the mid-point of reionization ($z_{\rm Re}$) from Planck (Planck Collaboration VI 2018).

As discussed in the previous section, the models disfavoured by the LOFAR upper limits are driven to produce a mid-point of reionization at $z \approx 9.1$. The full range of IGM neutral fractions disfavoured by LOFAR at $z \approx 9.1$ correspond to $0.15 \lesssim \bar{x}_{\rm H\,I} \lesssim 0.6$. Compared to the existing observational constraints, this places these disfavoured models at roughly $\gtrsim 2\sigma$. Unfortunately, owing to the still large amplitude of the LOFAR upper limits, and the correspondingly large uncertainties, we have verified that a joint analysis is entirely constrained by the existing limits. However, prospects for this will improve in the near future with the further processing of existing observational data and multiple frequency (redshift) limits.

Our constraints on $\bar{x}_{\rm H\,I}$ are broadly consistent with those presented by Ghara et al. (2020) and Mondal et al. (2020), with any differences being explained by different choices in adopted priors between the

[16]The peak amplitude of the 21-cm PS is actually strongly model dependent and need not occur at the mid-point of reionization. However, throughout we refer to the peak occurring near the mid-point of reionization purely for the purpose of making a generalized qualitative statement.

works. For Mondal et al. (2020), the disfavoured limits are $0.38 < \bar{x}_{\rm H\,I} < 0.72$, which are broadly consistent with our limits. The slight offset likely arises due to differences in the modelling of f_* and the minimum source mass contributing to reionization (see Section 3.1). For Ghara et al. (2020), the limits on $\bar{x}_{\rm H\,I}$ appear from two regions of parameter space (cf. their table 5): (i) 'cold' reionization ($0.40 < \bar{x}_{\rm H\,I} < 0.55$) and (ii) patchy X-ray heating ($\bar{x}_{\rm H\,I} > 0.92$). For (i), reionization must be ongoing *and* the IGM must be cold. Our results are consistent with (i), given that Ghara et al. (2020) assume a fixed $M_{\rm turn} = 10^9\,{\rm M}_\odot$ while also including a hard prior on the neutral fraction excluding values below 0.19, while we have a flat prior down to zero. For (ii), Ghara et al. (2020) require reionization to be in its infancy *and* X-ray heating to be dominated by luminous, highly biased ($M_h \geq 10^{10}\,{\rm M}_\odot$) sources with very soft SEDs ($E_0 = 0.2$ keV). We do not recover their (ii) because our prior on $M_{\rm turn}$ has a hard upper limit of $M_h \leq 10^{10}\,{\rm M}_\odot$.

3.2.2 *UV luminosity functions*

Unlike the reionization history which is constrained to be within a narrow range around $\bar{x}_{\rm H\,I} \approx 0.5$, the UV LFs are not strongly constrained by the LOFAR upper limits alone. Instead, they show extremely large scatter in the shapes and amplitudes, especially at the faint end. As such, we cannot simply provide a constrained range of plausible UV LFs as we did previously for the reionization history (shaded region of middle right-hand panel of Fig. 1). Therefore, in the six panels in the top right-hand of Fig. 1, we plot the UV luminosity functions at $z = 6$, 7, 8, 10, 12, and 15 for 500 randomly sampled models drawn from the full posterior which exceed the LOFAR upper limit. This is one of the advantages of using 21CMFAST in that the built-in parametrization is capable of directly outputting UV LFs.

We choose to compare these randomly sampled UV LFs against a small subset of unlensed UV LFs at $z = 6{-}8$ (orange circles; Bouwens et al. 2015, 2017) and at $z = 10$ (pink squares; Oesch et al. 2018). The vast majority of the UV LFs disfavoured by LOFAR are strongly disfavoured by the existing UV galaxy limits (up to two orders of magnitude larger in amplitude). Again, this is driven by models producing excessive amounts of ionizing photons to have reionization ~50 per cent complete by $z \approx 9.1$. While the UV LFs are independent of the number of ionizing photons, to achieve cold reionization at $z \approx 9.1$, we prefer to have both a high $f_{\rm esc}$ and high stellar-to-halo mass relation (see the $f_* - f_{\rm esc}$ panel in Fig. 1). Interestingly, unlike the existing constraints on the IGM neutral fraction, there appear to be several models in excess of the LOFAR limits which appear to be capable of producing UV LFs consistent with the observed ones. However, the vast majority are strongly inconsistent, owing to the relatively small statistical uncertainties on the observed UV LFs.

Once again, this highlights the fundamental value of observing the cosmic 21-cm signal. Constraints on the amplitude of the 21-cm PS are capable of providing limits on the underlying UV galaxy LFs, beyond what is capable from existing space telescopes. Our galaxy model, which has an average star formation time-scale evolving with redshift as the Hubble time (or analogously the halo dynamical time; equation 3), and a redshift-independent stellar-to-halo mass relation is capable of reproducing current observations of high-z (z 6–10) UV LFs (e.g. fig. 4 of Park et al. 2019). Moreover, these scaling relations are consistent with more sophisticated high-z SAMs (e.g. Mutch et al. 2016; Yung et al. 2019), as well as empirical scaling relations (e.g. Tacchella et al. 2018). Therefore, the fact that the UV LFs corresponding to the models inconsistent with the LOFAR observations are generally above the observed UV LFs is a significant result, highlighting that such models are already ruled out by current observations.

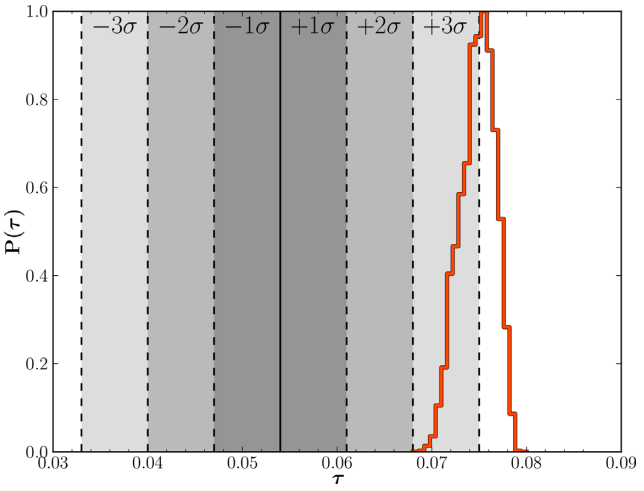

Figure 2. Histogram (red curve) of $\tau_{\rm e}$ from all models found to be in excess of the LOFAR upper limits on the 21-cm PS at $z \approx 9.1$. Shaded bands correspond to the statistical uncertainty on $\tau_{\rm e}$ as measured by Planck ($\tau_{\rm e} = 0.054 \pm 0.007$; Planck Collaboration VI 2018).

3.2.3 *Electron scattering optical depth, $\tau_{\rm e}$*

Next, in Fig. 2, we consider the electron scattering optical depth, $\tau_{\rm e}$, using the latest constraints from Planck ($\tau_{\rm e} = 0.054 \pm 0.007$; Planck Collaboration VI 2018). Here, the solid vertical line is the mean value from Planck, with shaded regions corresponding to being within $\pm1\sigma$, $\pm2\sigma$, $\pm3\sigma$ of the mean observed value. The red curve is the histogram of $\tau_{\rm e}$ obtained by binning all models disfavoured by the LOFAR upper limits. Clearly, all models in excess of LOFAR are $\gtrsim 2\sigma$ from existing observational constraints. Note again, this arises owing to the assumptions of our astrophysical source parametrization.[17] For example, allowing a strong redshift dependence on $f_{\rm esc}$ could produce models consistent with Planck. However, we note that most hydrodynamical simulations do not find evidence for a strong redshift evolution for $f_{\rm esc}$ (e.g. Kimm & Cen 2014; Paardekooper et al. 2015; Xu et al. 2016; Ma et al. 2020, though see Lewis et al. 2020). The primary driver of this is the requirement to have reionization at ~50 per cent by $z \sim 9.1$ for the 21-cm signal to exceed the current LOFAR limits, whereas the observed values from Planck prefer a redshift for the mid-point of $z_{\rm Re} = 7.67 \pm 0.5$ Planck Collaboration VI 2018).

In comparison, Mondal et al. (2020) recover disfavoured limits of $\tau_{\rm e} > 0.08$ at 68 per cent confidence, which is above the limit we recover (i.e. no models above $\tau_{\rm e} = 0.08$ in our work). This difference arises due to the fact that $\tau_{\rm e}$ is a free parameter that is allowed to reach $\tau_{\rm e} = 0.1$ in the Mondal et al. (2020) model. In our work, $\tau_{\rm e}$ is simply an output, given a specific parameter set. This emphasises the value of our direct galaxy parametrization as it allows for priors to be

[17] We note that our parametrization does allow for the *population averaged* $f_{\rm esc}$ to vary with redshift. This is because the halo mass function evolves with redshift, and we allow $f_{\rm esc}$ to scale with the halo mass through a power-law relation whose index, $\alpha_{\rm esc}$, is a free parameter. However, our range of priors on $\alpha_{\rm esc}$ results in a relatively modest redshift evolution of the population averaged galaxy $f_{\rm esc}$.

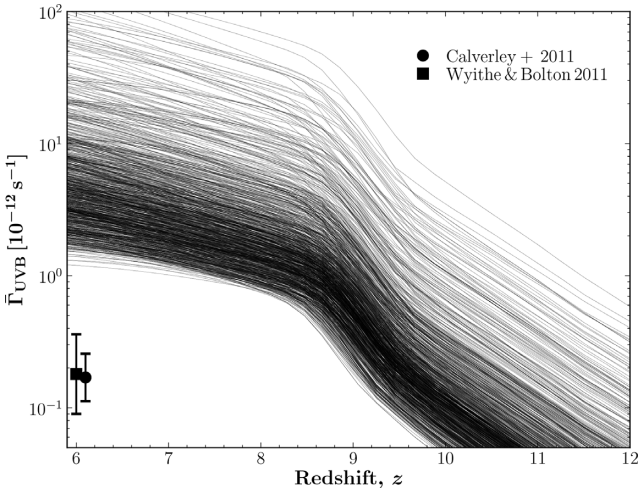

Figure 3. A comparison of the mean UV background radiation ($\bar{\Gamma}_{\rm UVB}$) from a random sample of 500 models drawn from the posterior (black curves) in excess of the LOFAR 21-cm PS upper limits against observed constraints from the proximity zones of high-z quasars (Calverley et al. 2011; Wyithe & Bolton 2011).

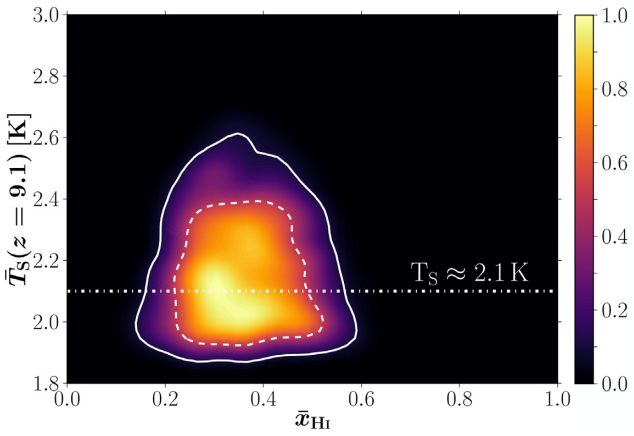

Figure 4. Two dimensional marginalized constraints on the IGM spin temperature, $T_{\rm S}$, and the IGM neutral fraction, $\bar{x}_{\rm H\,I}$. The white dashed (solid) contours correspond to the 68th (95th) percentiles while the horizontal white dot–dashed line corresponds to the value of the adiabatically cooled neutral IGM gas at mean density from RECFAST. The colour bar corresponds to a normalized probability for the models to be disfavoured by the LOFAR upper limits.

directly placed on physical quantities (e.g. $f_{\rm esc}$) rather than on derived quantities such as $\tau_{\rm e}$, which could conceivably result in non-physical models such as $f_{\rm esc} > 1$. Likely, by broadening our prior ranges (e.g. $M_{\rm turn}$), we would be able to produce similarly large optical depths. In any case, both works disfavour large $\tau_{\rm e}$.

3.2.4 Mean UV photo-ionization rate, $\bar{\Gamma}_{\rm UVB}$

In Fig. 3, we compare the mean UV background photoionization rate from 500 randomly sampled models from the posterior in excess of the LOFAR upper limits to observational constrains extracted from the proximity zones of $z > 6$ QSOs (e.g. Calverley et al. 2011; Wyithe & Bolton 2011). Here, the vast majority of the models ruled out by LOFAR are at least two orders of magnitude larger in amplitude than those inferred from the observational constraints ($\gtrsim 3\sigma$). This is consistent with the picture of an excessive amount of ionizing photons being required to ensure reionization is ∼50 per cent complete by $z \approx 9.1$. As a result, these models drastically overproduce the mean background photo-ionization rate.

3.3 Disfavoured IGM properties

Finally, we directly investigate the inferred limits on the IGM spin temperature from the models found to be in excess of the LOFAR upper limits at $z \approx 9.1$. Note, these are derived limits obtained by marginalizing over the full posterior of the model parameters. These limits are primarily driven by those models we rule out with extremely low soft-band X-ray luminosities (i.e. $\log_{10}(L_{\rm X<2\,keV}/{\rm SFR}) \lesssim 39.04$ from Section 3.1). In the absence of any heating source for the IGM, the neutral hydrogen gas will adiabatically cool. At $z \approx 9.1$, we infer this adiabatically cooled value for the neutral IGM gas at mean density to be $T_{\rm S} \approx 2.1\,{\rm K}$ (RECFAST; Seager, Sasselov & Scott 1999, 2000).

In Fig. 4, we provide the two dimensional marginalized posterior for the IGM spin temperature, $T_{\rm S}$ and the IGM neutral fraction, $\bar{x}_{\rm H\,I}$ after marginalizing over all parameters outlined in Section 2.2. The colour bar denotes the normalized probably for the models disfavoured by LOFAR, with larger probabilities highlighting regions more strongly disfavoured. The horizontal dot–dashed line corresponds to the value of the adiabatically cooled neutral IGM at mean density, $T_{\rm S} \approx 2.1\,{\rm K}$. Note, within 21CMFAST it is possible to have temperatures below $T_{\rm S} \approx 2.1\,{\rm K}$. This arises owing to adiabatic cooling and Compton heating in a non-uniform IGM. Due to non-linear structure evolution (i.e. more volume is in voids than overdensities) the volume weighted $T_{\rm S}$ can be below the limit at mean density (i.e. $T_{\rm S} \approx 2.1\,{\rm K}$). Fig. 4 implies that over a IGM neutral fraction of $0.15 \lesssim \bar{x}_{\rm H\,I} \lesssim 0.6$, the IGM spin temperature is disfavoured by LOFAR at 95 per cent confidence at $T_{\rm S} \lesssim 2.6\,{\rm K}$. This implies that the IGM must have undergone, at the bare minimum, the slightest amount of heating by X-rays.

Ghara et al. (2020) quote their own 95 per cent disfavoured limit on the IGM spin temperature of $T_{\rm S} \lesssim 2.9\,{\rm K}$ ($T_{\rm S} \lesssim 3.6\,{\rm K}$), from their uniform (non-uniform) IGM spin temperature models. For Mondal et al. (2020), their standard scenario (i.e. no excess radio background) results in a disfavoured limit of $T_{\rm S} \lesssim 10.1\,{\rm K}$ at 68 per cent confidence. Nevertheless, this limit is broadly consistent with our analysis, especially given the differences in the astrophysical models and parameters discussed previously.

4 CONCLUSION

Recently, LOFAR published new upper limits on the 21-cm PS from 141 h of data at $z \approx 9.1$ (Mertens et al. 2020). This corresponds to a factor ∼8 improvement over their best previous upper limit (Patil et al. 2017). Using 21CMMC, an MCMC sampler of 3D reionization simulations, we explore regions of astrophysical parameter space that are inconsistent with the observed limits. We directly forward-model the 3D cosmic 21-cm signal which includes: (i) a mass-dependent star formation rate and escape fraction to be able to self-consistently produce UV LFs, (ii) inhomogeneous recombinations, (iii) the evolution of the inhomogeneous IGM spin temperature, and (iv) an on-the-fly ionizing photon non-conservation corrections.

In terms of the astrophysical parameters responsible for reionization, we find that the upper limits presented by LOFAR are able to primarily limit the X-ray luminosity of the first sources. At 95 per cent confidence, LOFAR disfavours the soft-band X-ray luminosity, $L_{\rm X<2\,keV}/{\rm SFR}$ to $\log_{10}(L_{\rm X<2\,keV}/{\rm SFR}) \lesssim 39.04$. These

limits currently sit below expectations from local populations of star-forming galaxies (Mineo et al. 2012), stacked *Chandra* observations (Lehmer et al. 2016) and predictions at high-redshifts by population synthesis models (Fragos et al. 2013a). Nevertheless, this implies that the X-ray background must have been sufficiently large to provide some level of heating to the IGM.

For the UV galaxy properties, we find that the regions disfavoured by LOFAR are heavily tied to the observational redshift of $z \approx 9.1$. That is, to be able to exceed the LOFAR upper limit, reionization must have been $\sim$50 per cent complete to maximize the amplitude of the 21-cm PS. As such, the LOFAR upper limits disfavour the normalizations of the mass dependent star formation rate, $f_{*,10}$ and escape fraction, $f_{\rm esc,10}$, to be above $\sim$3.1 and $\sim$2.3 per cent, respectively. Finally, a minimum source mass above $\log_{10}(M_{\rm turn}) \gtrsim 8.13$ is disfavoured at 95 per cent confidence. This shows the value of having tools such as 21CMMC to perform forward modelling of the cosmic 21-cm signal to be able to infer the astrophysics from observations of the 21-cm signal in a fully Bayesian framework. Note however, this interpretation is specific to our astrophysical parametrization.

To highlight the advantage of using 21CMMC, we then compared the models disfavoured by the LOFAR upper limits against a range of existing observation constraints within the literature. We compared against: (i) observational constraints and limits on the IGM neutral fraction, (ii) the observed UV LFs at $z = 6$, 7, 8, and 10, (iii) the electron scattering optical depth and (iv) the mean UV background photoionization rate. In most instances, the astrophysical models disfavoured by LOFAR were inconsistent with existing observational constraints by $\gtrsim 2\sigma$.

Finally, we explored limits on the IGM spin temperature, $T_{\rm S}$, due to the lack of X-ray heating inferred in the models disfavoured by LOFAR. Over an IGM neutral fraction range of $0.15 \lesssim \bar{x}_{\rm HI} \lesssim 0.6$, the LOFAR upper limits imply a 95 per cent confidence limit of $T_{\rm S} \gtrsim 2.6$ K. In comparison, the adiabatically cooled limit at $z \approx 9.1$ is $T_{\rm S} \approx 2.1$ K (at mean density), which implies the IGM must have undergone some level of X-ray heating. This interpretation is consistent with the results presented by both Ghara et al. (2020) and Mondal et al. (2020) and provides a consistency check that the recovered bulk IGM properties from the current LOFAR limits are insensitive to the details of the modelling, including the type of seminumerical simulation, galaxy parametrization, and use of emulators in the MCMC.

With the amplitude of the existing limits on the 21-cm PS presented by LOFAR still being relatively large and only at a single observed frequency, this limits our ability to constrain the astrophysics of the sources responsible for reionization. However, in the near future, these limits will continue to reduce in amplitude as LOFAR processes more observational data and improves their analysis pipeline, while at the same time also providing multiple frequency limits. Using the framework showcased here, these upcoming limits can start ruling out otherwise viable galaxy evolution models.

ACKNOWLEDGEMENTS

We thank the anonymous referee for their constructive feedback which has improved this manuscript. Parts of this research were supported by the Australian Research Council Centre of Excellence for All Sky Astrophysics in Three Dimensions (ASTRO 3D), through project number CE170100013. AM acknowledges funding support from the European Research Council (ERC) under the European Union's Horizon 2020 research and innovation programme (grant agreement no. 638809 – AIDA – PI: AM). FGM and LVEK would like to acknowledge support from an SKA-NL Roadmap grant from the Dutch Ministry of Education, Culture and Science. GM is thankful for support by Swedish Research Council grant 2016-03581. SZ acknowledges support from the Israeli Science Foundation (grant no. 255/18). ITI was supported by the Science and Technology Facilities Council [grant numbers ST/I000976/1 and ST/T000473/1] and the Southeast Physics Network (SEP-Net). AG would like to acknowledge IUCAA, Pune for providing support through the associateship programme. RM is grateful for financial support from the Wenner-Gren Foundations.

DATA AVAILABILITY

The data underlying this article will be shared on reasonable request to the corresponding author.

REFERENCES

Akeret J., Seehars S., Amara A., Refregier A., Csillaghy A., 2013, Astron. Comput., 2, 27
Ali Z. S. et al., 2015, ApJ, 809, 61
Barkana R., 2016, Phys. Rep., 645, 1
Barkana R., Loeb A., 2001, Phys. Rep., 349, 125
Barkana R., Loeb A., 2005, ApJ, 626, 1
Barone-Nugent R. L. et al., 2014, ApJ, 793, 17
Barry N. et al., 2019, ApJ, 884, 1
Basu-Zych A. R. et al., 2013, ApJ, 774, 152
Beardsley A. P. et al., 2016, ApJ, 833, 102
Behroozi P. S., Silk J., 2015, ApJ, 799, 32
Behroozi P., Wechsler R. H., Hearin A. P., Conroy C., 2019, MNRAS, 488, 3143
Bernardi G. et al., 2016, MNRAS, 461, 2847
Bouwens R. J. et al., 2015, ApJ, 803, 34
Bouwens R. J., Oesch P. A., Illingworth G. D., Ellis R. S., Stefanon M., 2017, ApJ, 843, 129
Bowman J. D., Rogers A. E. E., 2010, Nature, 468, 796
Bowman J. D., Rogers A. E. E., Monsalve R. A., Mozdzen T. J., Mahesh N., 2018a, Nature, 555, 67
Bowman J. D., Rogers A. E. E., Monsalve R. A., Mozdzen T. J., Mahesh N., 2018b, Nature, 564, E35
Bradley R. F., Tauscher K., Rapetti D., Burns J. O., 2019, ApJ, 874, 153
Brorby M., Kaaret P., Prestwich A., 2014, MNRAS, 441, 2346
Brorby M., Kaaret P., Prestwich A., Mirabel I. F., 2016, MNRAS, 457, 4081
Calverley A. P., Becker G. D., Haehnelt M. G., Bolton J. S., 2011, MNRAS, 412, 2543
Cheng C. et al., 2018, ApJ, 868, 26
Choudhury T. R., Paranjape A., 2018, MNRAS, 481, 3821
Das A., Mesinger A., Pallottini A., Ferrara A., Wise J. H., 2017, MNRAS, 469, 1166
Davies F. B. et al., 2018, ApJ, 864, 142
Dayal P., Ferrara A., Dunlop J. S., Pacucci F., 2014, MNRAS, 445, 2545
DeBoer D. R. et al., 2017, PASP, 129, 045001
Dillon J. S. et al., 2015, Phys. Rev. D, 91, 123011
Douna V. M., Pellizza L. J., Mirabel I. F., Pedrosa S. E., 2015, A&A, 579, A44
Draine B. T., Miralda-Escudé J., 2018, ApJ, 858, L10
Eastwood M. W. et al., 2019, AJ, 158, 84
Eide M. B., Graziani L., Ciardi B., Feng Y., Kakiichi K., Di Matteo T., 2018, MNRAS, 476, 1174
Field G. B., 1958, Proc. Inst. Radio Eng., 46, 240
Foreman-Mackey D., Hogg D. W., Lang D., Goodman J., 2013, PASP, 125, 306
Fragos T. et al., 2013a, ApJ, 764, 41
Fragos T., Lehmer B. D., Naoz S., Zezas A., Basu-Zych A., 2013b, ApJ, 776, L31
Furlanetto S. R., Oh S. P., Briggs F. H., 2006, Phys. Rep., 433, 181
Gehlot B. K. et al., 2019, MNRAS, 488, 4271

Gehlot B. K., et al., 2020, MNRAS, 499, 4158
Ghara R., Choudhury T. R., Datta K. K., 2015, MNRAS, 447, 1806
Ghara R., Mellema G., Giri S. K., Choudhury T. R., Datta K. K., Majumdar S., 2018, MNRAS, 476, 1741
Ghara R. et al., 2020, MNRAS, 493, 4728
Giroux M. L., Sutherland R. S., Shull J. M., 1994, ApJ, 435, L97
Gnedin N. Y., Kaurov A. A., 2014, ApJ, 793, 30
Goodman J., Weare J., 2010, Commun. Appl. Math. Comput. Sci., 5, 65
Greenhill L. J., Bernardi G., 2012, preprint (arXiv:1201.1700)
Greig B., Mesinger A., 2015, MNRAS, 449, 4246
Greig B., Mesinger A., 2017, MNRAS, 472, 2651
Greig B., Mesinger A., 2018, MNRAS, 477, 3217
Greig B., Mesinger A., Pober J. C., 2016, MNRAS, 455, 4295
Greig B., Mesinger A., Haiman Z., Simcoe R. A., 2017, MNRAS, 466, 4239
Greig B., Mesinger A., Bañados E., 2019, MNRAS, 484, 5094
Gupta Y. et al., 2017, Curr. Sci., 113, 707
Harikane Y. et al., 2016, ApJ, 821, 123
Hassan S., Davé R., Finlator K., Santos M. G., 2017, MNRAS, 468, 122
Hills R., Kulkarni G., Meerburg P. D., Puchwein E., 2018, Nature, 564, E32
Hoag A. et al., 2019, ApJ, 878, 12
Hui L., Gnedin N. Y., 1997, MNRAS, 292, 27
Hutter A., 2018, MNRAS, 477, 1549
Hutter A., Dayal P., Yepes G., Gottlöber S., Legrand L., Ucci G., 2020, preprint (arXiv:2004.08401)
Jensen H. et al., 2013, MNRAS, 435, 460
Katz H., Kimm T., Haehnelt M., Sijacki D., Rosdahl J., Blaizot J., 2018, MNRAS, 478, 4986
Kimm T., Cen R., 2014, ApJ, 788, 121
Kimm T., Katz H., Haehnelt M., Rosdahl J., Devriendt J., Slyz A., 2017, MNRAS, 466, 4826
Kolopanis M. et al., 2019, ApJ, 883, 133
Koopmans L. et al., 2015, Proceedings of AASKA14, , Giardini Naxos, Italy
Kuhlen M., Faucher-Giguère C.-A., 2012, MNRAS, 423, 862
Lacey C., Cole S., 1993, MNRAS, 262, 627
Lehmer B. D. et al., 2016, ApJ, 825, 7
Lewis J. S. W. et al., 2020, MNRAS, 496, 4342
Li W. et al., 2019, ApJ, 887, 141
Lidz A., Zahn O., McQuinn M., Zaldarriaga M., Hernquist L., 2008, ApJ, 680, 962
Ma X., Quataert E., Wetzel A., Hopkins P. F., Faucher-Giguère C.-A., Kereš D., 2020, MNRAS, 498, 2001
Madau P., Fragos T., 2017, ApJ, 840, 39
Mao Y., Shapiro P. R., Mellema G., Iliev I. T., Koda J., Ahn K., 2012, MNRAS, 422, 926
Mason C. A., Trenti M., Treu T., 2015, ApJ, 813, 21
Mason C. A., Treu T., Dijkstra M., Mesinger A., Trenti M., Pentericci L., de Barros S., Vanzella E., 2018, ApJ, 856, 2
Mason C. A. et al., 2019, MNRAS, 485, 3947
McGreer I. D., Mesinger A., D'Odorico V., 2015, MNRAS, 447, 499
McQuinn M., 2012, MNRAS, 426, 1349
McQuinn M., Furlanetto S. R., Hernquist L., Zahn O., Zaldarriaga M., 2005, ApJ, 630, 643
Mellema G., Iliev I. T., Pen U.-L., Shapiro P. R., 2006, MNRAS, 372, 679
Mellema G. et al., 2013, Exp. Astron., 36, 235
Mertens F. G. et al., 2020, MNRAS, 493, 1662
Mesinger A., Dijkstra M., 2008, MNRAS, 390, 1071
Mesinger A., Furlanetto S., 2007, ApJ, 669, 663
Mesinger A., Furlanetto S., Cen R., 2011, MNRAS, 411, 955
Mesinger A., Ferrara A., Spiegel D. S., 2013, MNRAS, 431, 621
Mesinger A., Ewall-Wice A., Hewitt J., 2014, MNRAS, 439, 3262
Mesinger A., Aykutalp A., Vanzella E., Pentericci L., Ferrara A., Dijkstra M., 2015, MNRAS, 446, 566
Mesinger A., Greig B., Sobacchi E., 2016, MNRAS, 459, 2342
Mineo S., Gilfanov M., Sunyaev R., 2012, MNRAS, 419, 2095
Mirocha J., 2019, preprint (arXiv:1909.12595)
Mirocha J., 2020, MNRAS, 499, 4534
Mirocha J., Furlanetto S. R., Sun G., 2017, MNRAS, 464, 1365
Mitra S., Choudhury T. R., Ferrara A., 2015, MNRAS, 454, L76
Mitra S., Choudhury T. R., Ferrara A., 2018, MNRAS, 473, 1416
Molaro M., Davé R., Hassan S., Santos M. G., Finlator K., 2019, MNRAS, 489, 5594
Mondal R., Bharadwaj S., Majumdar S., 2017, MNRAS, 464, 2992
Mondal R. et al., 2020, MNRAS, 498, 4178
Monsalve R. A., Rogers A. E. E., Bowman J. D., Mozdzen T. J., 2017, ApJ, 847, 64
Monsalve R. A., Greig B., Bowman J. D., Mesinger A., Rogers A. E. E., Mozdzen T. J., Kern N. S., Mahesh N., 2018, ApJ, 863, 11
Monsalve R. A., Fialkov A., Bowman J. D., Rogers A. E. E., Mozdzen T. J., Cohen A., Barkana R., Mahesh N., 2019, ApJ, 875, 67
Morales M. F., Wyithe J. S. B., 2010, ARA&A, 48, 127
Mutch S. J., Geil P. M., Poole G. B., Angel P. W., Duffy A. R., Mesinger A., Wyithe J. S. B., 2016, MNRAS, 462, 250
Ocvirk P. et al., 2016, MNRAS, 463, 1462
Oesch P. A., Bouwens R. J., Illingworth G. D., Labbé I., Stefanon M., 2018, ApJ, 855, 105
Okamoto T., Gao L., Theuns T., 2008, MNRAS, 390, 920
Paardekooper J.-P., Khochfar S., Vecchia C. D., 2015, MNRAS, 451, 2544
Paciga G. et al., 2013, MNRAS, 433, 639
Pacucci F., Mesinger A., Mineo S., Ferrara A., 2014, MNRAS, 443, 678
Paranjape A., Choudhury T. R., 2014, MNRAS, 442, 1470
Paranjape A., Choudhury T. R., Padmanabhan H., 2016, MNRAS, 460, 1801
Park J., Mesinger A., Greig B., Gillet N., 2019, MNRAS, 484, 933
Parsons A. R. et al., 2010, AJ, 139, 1468
Parsons A. R. et al., 2014, ApJ, 788, 106
Patil A. H. et al., 2017, ApJ, 838, 65
Patra N., Subrahmanyan R., Sethi S., Shankar N. U., Raghunathan A., 2015, ApJ, 801, 138
Philip L. et al., 2019, J. Astron. Instrum., 8, 1950004
Planck Collaboration XIII, 2016, A&A, 594, 63
Planck Collaboration et al., 2018, A&A, 641, 73
Pober J. C. et al., 2015, ApJ, 809, 62
Pritchard J. R., Furlanetto S. R., 2007, MNRAS, 376, 1680
Pritchard J. R., Loeb A., 2012, Rep. Prog. Phys., 75, 086901
Qin Y. et al., 2017, MNRAS, 472, 2009
Ricci F., Marchesi S., Shankar F., La Franca F., Civano F., 2017, MNRAS, 465, 1915
Ricotti M., Ostriker J. P., 2004, MNRAS, 350, 539
Ross H. E., Dixon K. L., Iliev I. T., Mellema G., 2017, MNRAS, 468, 3785
Salpeter E. E., 1955, ApJ, 121, 161
Scoccimarro R., 1998, MNRAS, 299, 1097
Seager S., Sasselov D. D., Scott D., 1999, ApJ, 523, L1
Seager S., Sasselov D. D., Scott D., 2000, ApJS, 128, 407
Shapiro P. R., Giroux M. L., Babul A., 1994, ApJ, 427, 25
Shaw A. K., Bharadwaj S., Mondal R., 2020, MNRAS, 498, 1480
Sheth R. K., Tormen G., 1999, MNRAS, 308, 119
Singh S., Subrahmanyan R., 2019, ApJ, 880, 26
Singh S. et al., 2017, ApJ, 845, L12
Sobacchi E., Mesinger A., 2013a, MNRAS, 432, L51
Sobacchi E., Mesinger A., 2013b, MNRAS, 432, 3340
Sobacchi E., Mesinger A., 2014, MNRAS, 440, 1662
Sobacchi E., Mesinger A., 2015, MNRAS, 453, 1843
Sokolowski M. et al., 2015, PASA, 32, e004
Springel V., Hernquist L., 2003, MNRAS, 339, 312
Sun G., Furlanetto S. R., 2016, MNRAS, 460, 417
Tacchella S., Bose S., Conroy C., Eisenstein D. J., Johnson B. D., 2018, ApJ, 868, 92
Tingay S. J. et al., 2013, PASA, 30, 7
Trott C. M. et al., 2020, MNRAS, 493, 4711
van Haarlem M. P. et al., 2013, A&A, 556, 2
Voytek T. C., Natarajan A., García J. M. J., Peterson J. B., López-Cruz O., 2014, ApJ, 782, L9
Wayth R. et al., 2018, PASA, 35, 33
Wise J. H., Demchenko V. G., Halicek M. T., Norman M. L., Turk M. J., Abel T., Smith B. D., 2014, MNRAS, 442, 2560

Wouthuysen S. A., 1952, AJ, 57, 31
Wyithe J. S. B., Bolton J. S., 2011, MNRAS, 412, 1926
Xu H., Wise J. H., Norman M. L., Ahn K., O'Shea B. W., 2016, ApJ, 833, 84
Yue B., Ferrara A., Xu Y., 2016, MNRAS, 463, 1968
Yung L. Y. A., Somerville R. S., Popping G., Finkelstein S. L., Ferguson H. C., Davé R., 2019, MNRAS, 490, 2855
Zahn O., Lidz A., McQuinn M., Dutta S., Hernquist L., Zaldarriaga M., Furlanetto S. R., 2007, ApJ, 654, 12
Zahn O., Mesinger A., McQuinn M., Trac H., Cen R., Hernquist L. E., 2011, MNRAS, 414, 727
Zarka P., Girard J. N., Tagger M., Denis L., 2012, in Boissier S., de Laverny P., Nardetto N., Samadi R., Valls-Gabaud D., Wozniak H., eds, SF2A-2012: Proceedings of the Annual Meeting of the French Society of Astronomy and Astrophysics, p. 687
Zaroubi S., 2013, Astrophysics and Space Science Library, Vol. 396, The First Galaxies, Springer-Verlag, Berlin, p. 45

This paper has been typeset from a TEX/LATEX file prepared by the author.